Gamma-ray vortices emitted from nonlinear inverse Thomson scattering of a two-wavelength laser beam

Yoshitaka Taira[1,*] and Masahiro Katoh[2]

[1]*Research Institute for Measurement and Analytical Instrumentation, National Metrology Institute of Japan,*
National Institute of Advanced Industrial Science and Technology (AIST), Tsukuba 305-8568, Japan
[2]*Institute for Molecular Science, National Institutes of Natural Sciences/School of Physical Sciences,*
SOKENDAI (The Graduate University for Advanced Studies), Okazaki 444-8585, Japan

We develop a classical theory of nonlinear inverse Thomson scattering of a two-wavelength laser beam, which is valid for laser beams with linear or circular polarization and arbitrary intensity and wavelength. We reveal that an electron inside a circularly polarized two-wavelength laser field undergoes a cycloid motion in the transverse plane and radiates an electromagnetic wave forming a spiral phase structure. Its photon energy is proportional to a linear combination of the product between the initial laser photon energies $\hbar\omega_{01}$ and $\hbar\omega_{02}$, and their harmonic numbers n_1 and n_2, namely, $n_1\hbar\omega_{01} + n_2\hbar\omega_{02}$. The orbital angular momentum of a photon due to the spiral phase structure is given by $(n_1 + n_2 \pm 1)\hbar$. We show that a combination of two wavelengths differing by one order of magnitude or more is advantageous for producing gamma rays carrying a large orbital angular momentum of $\sim 10\hbar$. Moreover, this work indicates that a helical undulator with two magnetic periods is capable of producing photons with a large orbital angular momentum. This radiation process plays an important role in the development of optical vortex beams and even in astrophysical environments.

I. INTRODUCTION

An optical vortex forming a helical wave front has a spiral phase structure of $\exp(im\phi)$, where m is an integer called the topological charge and ϕ is the azimuthal angle in the plane transverse to the propagation axis [1]. An important characteristic of an optical vortex is that it has an annular intensity distribution in the transverse plane associated with a phase singularity. In 1992, Allen *et al.* pointed out that an optical vortex with a spiral phase term has orbital angular momentum (OAM) equal to $m\hbar$ around the propagation axis in addition to spin angular momentum (SAM), where $\hbar$ is the Planck constant divided by 2π [2,3].

Fundamental and applied studies on optical vortices using visible wavelength lasers are ongoing [4,5]. Recent theoretical works show that optical vortices at ultraviolet, x-ray, and MeV gamma-ray frequencies likely trigger new phenomena in photoionization [6], a dichroic effect [7], Thomson and Compton scattering [8–11], photodisintegration [12], and photonuclear reactions [13]. The highest photon energy of optical vortices ever generated is 9–25 keV using synchrotron radiation [14–20]. The generation of higher-energy x-ray and gamma-ray vortices is challenging, and extensive research is ongoing. Recently, it has been proposed that gamma-ray vortices can be produced using optical vortex lasers via inverse Compton scattering [21,22] and laser-plasma interactions [23].

We proposed another method to produce high-energy vortex photons based on nonlinear inverse Thomson scattering (NITS) of a circularly polarized intense laser beam [13].

Inverse Thomson scattering occurs when a relativistic electron interacts with a laser photon and a high-energy photon is backscattered. Here we consider that inverse Thomson scattering is a scattering process where the energy of the scattered photon is much smaller than the initial electron energy. When an electron interacts with an intense laser beam characterized by a laser strength parameter $a_0 \geqslant 1$, the nonlinear effect of the inverse Thomson scattering becomes prominent, and higher harmonic photons are emitted. In NITS with a circularly polarized intense laser beam, the mth harmonic gamma rays have a spiral phase term $\exp\{i(m-1)\phi\}$ and have OAM equal to $(m-1)\hbar$ [13]. The transverse circular motion of an electron induced by a circularly polarized laser beam is essential for producing gamma-ray vortices [24]. Our previous theoretical work is supported by an experimental result, which shows the annular intensity distribution of second-harmonic x rays generated from NITS of a circularly polarized laser beam [25].

The efficiency of NITS in generating gamma-ray vortices seems to be higher than the method using inverse Compton scattering of optical vortex laser beams [21], roughly by the Lorentz factor for an electron, which is typically ~ 1000 [13]. Although laser-plasma interactions require an extremely intense laser beam with $a_0 > 100$ to generate gamma-ray vortices [23], NITS can produce gamma-ray vortices using less intense laser beams with $a_0 \sim 1$.

In inverse Thomson scattering, when a 1 eV photon is backscattered by a 1 GeV electron, an ~ 10 MeV photon is produced. The scattered gamma rays have a tunable energy, high intensity, and a short pulse, and are quasimonochromatic and highly polarized. Gamma-ray sources based on inverse Thomson scattering have been investigated and utilized in
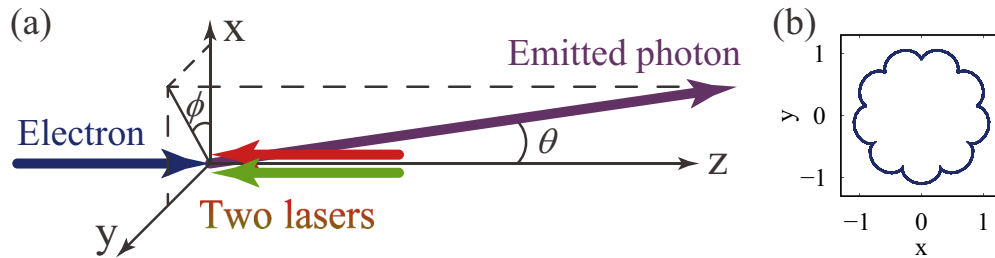
---
*yoshitaka-taira@aist.go.jp

FIG. 1. (a) Coordinate system used to calculate NITS for a two-wavelength laser beam. (b) Typical transverse electron motion induced by a two-wavelength laser beam circularly polarized in the x-y plane.

various research fields. Uses include the nondestructive measurement of industrial products [26], nuclear physics [27], electron beam diagnostics [28–30], detection of nanometer-scale vacancies inside a thick material [31–33], and generation of polarized positron beams for a linear collider [34]. Inverse Thomson scattering and Compton scattering in the nonlinear region have been theoretically investigated in several works as sources of x rays and gamma rays, not only in laboratories but also in astrophysical situations [35–50]. The development of high-power lasers has enabled experimental studies of NITS using an electron accelerator [25,51–54] and laser wakefield acceleration [55–58]. Although a previous work on NITS studied a single-wavelength laser beam, Sakai *et al.* theoretically investigated NITS for a linearly polarized two-wavelength laser beam [59]. They showed that an electron has a superimposed trajectory in the two-color laser beam and it emits photons with a multipeaked energy spectrum.

In this paper, we develop a theory to describe NITS for a two-wavelength laser beam, which is applicable to an electron with arbitrary energy and to a laser beam with linear or circular polarization and arbitrary intensity and wavelength. Explicit expressions for the electric fields, energy, intensity distributions, and the number of scattered photons are derived and numerically evaluated. Compared with a previous work [59], which has only investigated linearly polarized laser beams and has not addressed OAM of emitted photons, our current work shows that an electron inside two circularly polarized laser beams has a cycloid trajectory in the plane transverse to the direction of motion and photons emitted from such an electron have a spiral phase term and OAM. It has been demonstrated that photons emitted from an electron obeying a circular trajectory have a spiral phase term and OAM [24]. Here, we show that optical vortices can be generated from the cycloid motion of an electron. We show that a combination of two wavelengths differing by one order of magnitude or more is advantageous for producing intense gamma rays with a relatively large OAM of $\sim 10\hbar$, in contrast to NITS using a one-wavelength laser beam in which the number of photons rapidly decreases with increasing OAM. Our theory will pave the way for the generation of high-energy photons with large OAM from relativistic electrons, which will provide research opportunities in laser physics, atomic physics, nuclear physics, high-energy physics, astrophysics, and material sciences.

This paper is organized as follows. In Sec. II, we derive theoretical equations for the electron motion and scattered radiation field for two laser beams with linear or circular

polarization. In Sec. III, we show the results of our numerical calculation and discuss the properties of the scattered radiation field for circularly polarized lasers. In Sec. IV, we discuss the optimum laser parameters to produce intense gamma rays with a large OAM.

II. THEORY

A. Electron trajectory inside a two-wavelength laser beam

We assume that an electron moves along the z axis, that the two laser beams simultaneously propagate in the $-z$ direction, and that one photon is emitted from the electron in a direction with an angle θ with respect to the z axis and an angle ϕ with respect to the x axis, as shown in Fig. 1(a). To simplify the calculation, we assume that the electron and the lasers interact head-on. Inverse Thomson scattering of a two-wavelength laser beam in the linear region has been investigated [60–62]. In this paper, we treat the radiation process of NITS in which one photon is emitted via an interaction between the electron and the two laser beams.

The normalized vector potential, $\mathbf{a} = (a_x, a_y)$, of a two-wavelength laser beam is defined as

$$\mathbf{a} = \left\{ \frac{a_{01}}{\sqrt{2}} \sqrt{1 + \delta_{01}} \cos(k_{01}\eta) + \frac{a_{02}}{\sqrt{2}} \sqrt{1 + \delta_{02}} \cos(k_{02}\eta) \right\} \mathbf{e}_x$$
$$+ \left\{ \frac{a_{01}}{\sqrt{2}} \sqrt{1 - \delta_{01}} \sin(k_{01}\eta) + \frac{a_{02}}{\sqrt{2}} \sqrt{1 - \delta_{02}} \sin(k_{02}\eta) \right\} \mathbf{e}_y.$$

(1)

Here, a_0 is a dimensionless laser strength parameter, $a_0 = 0.855 \times 10^{-9} \lambda_0 (\mu m) I_0^{1/2} (\text{W/cm}^2)$, where $\lambda_0 = 2\pi/k_0$, k_0, and I_0 are the wavelength, the wave number, and the intensity of the laser, respectively. $\delta_0 = 0$ for circular polarization and $\delta_0 = 1$ for linear polarization (and additional subscripts 1 and 2 indicate the first laser and the second laser, respectively). $\eta = z + ct$ is an independent variable. c is the speed of light, t is time, and $\mathbf{e}_x$ and $\mathbf{e}_y$ are the unit vectors along the x and y axes, respectively. In Eq. (1), we consider cases where the major polarization axes of the two laser beams coincide. Although the following mathematical approach can be applied to more general cases, to simplify the analytic expressions, we restrict the analysis to the conditions given above, which may be applicable to many practical applications. For the same reason, the handedness of circular polarization and the initial phases of two laser beams are considered to be the same in Eq. (1). The former will be discussed later and the latter in Appendix B.

The electron momentum normalized by the electron rest energy during the interaction with the laser is $\mathbf{u} = \gamma\boldsymbol{\beta}$, where γ and $\boldsymbol{\beta}$ are the Lorentz factor and the normalized velocity of the electron, respectively. The vector components of $\mathbf{u}$ can be derived by solving the relativistic Lorentz equations [44]: $u_x = a_x$, $u_y = a_y$, and

$$u_z = \frac{\gamma_0^2(1+\beta_0)^2 - 1 - \left(u_x^2 + u_y^2\right)}{2\gamma_0(1+\beta_0)}. \tag{2}$$

Here, $\gamma_0 = 1/\sqrt{1-\beta_0^2}$ and β_0 are the Lorentz factor and the normalized velocity of the electron before the interaction, respectively.

The electron orbits, $\mathbf{r}_e = (x_e, y_e, z_e)$, are derived using the relation $d\mathbf{r}_e/d\eta = \mathbf{u}/\{\gamma_0(1+\beta_0)\}$ [44]:

$$x_e = r_{01}\sqrt{1+\delta_{01}}\sin(k_{01}\eta) + r_{02}\sqrt{1+\delta_{02}}\sin(k_{02}\eta) + x_0, \tag{3}$$

$$y_e = -r_{01}\sqrt{1-\delta_{01}}\cos(k_{01}\eta) - r_{02}\sqrt{1-\delta_{02}}\cos(k_{02}\eta) + y_0, \tag{4}$$

and

$$\begin{aligned} z_e = {}&\beta_{12}\eta - z_{01}\delta_{01}\sin(2k_{01}\eta) - z_{02}\delta_{02}\sin(2k_{02}\eta) \\ &- \tfrac{1}{2}z_{012}^{(-)}\{\sqrt{(1+\delta_{01})(1+\delta_{02})} \\ &+ \sqrt{(1-\delta_{01})(1-\delta_{02})}\}\sin(k_{01}\eta - k_{02}\eta) \\ &- \tfrac{1}{2}z_{012}^{(+)}\{\sqrt{(1+\delta_{01})(1+\delta_{02})} \\ &- \sqrt{(1-\delta_{01})(1-\delta_{02})}\}\sin(k_{01}\eta + k_{02}\eta) + z_0. \end{aligned} \tag{5}$$

Here, x_0, y_0, and z_0 are the initial positions of the electron along the x, y, and z axes, respectively, and the other parameters are given by

$$r_{01,02} = \frac{a_{01,02}}{\sqrt{2}\gamma_0(1+\beta_0)k_{01,02}}, \tag{6}$$

$$\beta_{12} = \frac{\gamma_0^2(1+\beta_0)^2 - 1 - \left(a_{01}^2 + a_{02}^2\right)/2}{2\gamma_0^2(1+\beta_0)^2}, \tag{7}$$

$$z_{01,02} = \frac{a_{01,02}^2}{8\gamma_0^2(1+\beta_0)^2 k_{01,02}}, \tag{8}$$

and

$$z_{012}^{(\pm)} = \frac{a_{01}a_{02}}{2\gamma_0^2(1+\beta_0)^2(k_{01}\pm k_{02})}. \tag{9}$$

B. Scattered radiation field

1. General expression

The electric field emitted by a single electron in an arbitrary trajectory and velocity can be calculated from the Lienard-Wiechert potentials (Sec. 14.5 in [63]). The Fourier component of the electric field is

$$\mathbf{E} = -i\sqrt{\frac{e^2k^2}{32\pi^3\epsilon_0^2}}\frac{e^{ikR}}{R}$$
$$\times \int_{-\infty}^{\infty} dt\{\mathbf{n}\times(\mathbf{n}\times\boldsymbol{\beta})\}e^{ik\{ct-\mathbf{n}\cdot\mathbf{r}_e(t)\}}, \tag{10}$$

where e is the elementary charge. $k = \omega/c$ and ω are the wave number and the angular frequency of the emitted photon, respectively. ϵ_0 is the permittivity of a vacuum, R is the distance from the origin to the observation point, $\mathbf{n}$ is a unit vector pointing from the origin to the observation point, and $\mathbf{r}_e$ is the electron orbit described in Eqs. (3)–(5). Equation (10) can be written using the spherical coordinate system (r, θ, ϕ) with unit vectors $(\mathbf{e}_r, \mathbf{e}_\theta, \mathbf{e}_\phi)$ as in [45,64] as follows:

$$E_\theta = i\sqrt{\frac{e^2k^2}{32\pi^3\epsilon_0^2c^2}}\frac{e^{ikR}}{R}\int_{-\eta_0}^{\eta_0} d\eta \frac{d\mathbf{r}_e}{d\eta}\cdot\mathbf{e}_\theta e^{i\psi} \tag{11}$$

and

$$E_\phi = i\sqrt{\frac{e^2k^2}{32\pi^3\epsilon_0^2c^2}}\frac{e^{ikR}}{R}\int_{-\eta_0}^{\eta_0} d\eta \frac{d\mathbf{r}_e}{d\eta}\cdot\mathbf{e}_\phi e^{i\psi}. \tag{12}$$

Here, $\psi \equiv k\{ct - \mathbf{n}\cdot\mathbf{r}_e(t)\}$, $\eta_0 = N_{01}\lambda_{01}/2 = N_{02}\lambda_{02}/2$, and N_{01} and N_{02} are the number of periods of the two laser beams interacting with the single electron. The variable $2\eta_0$ corresponds to the longitudinal pulse width of the two laser beams [44]. Here, we assume that the pulse widths of the two laser beams are the same. The unit vectors $(\mathbf{e}_r, \mathbf{e}_\theta, \mathbf{e}_\phi)$ are given by Eqs. (23a)–(23c) in [44].

2. Circular polarization for both laser beams

In the following calculation, we assume that both laser beams are circularly polarized, which we will see is the best way to produce optical vortices with a large OAM. Other polarization states are discussed later and in Appendix A. When both laser beams are circularly polarized ($\delta_{01} = \delta_{02} = 0$), the electron orbits can be expressed using Eqs. (3)–(5):

$$x_e = r_{01}\sin(k_{01}\eta) + r_{02}\sin(k_{02}\eta) + x_0, \tag{13}$$

$$y_e = -r_{01}\cos(k_{01}\eta) - r_{02}\cos(k_{02}\eta) + y_0, \tag{14}$$

and

$$z_e = \beta_{12}\eta - z_{012}^{(-)}\sin(k_{01}\eta - k_{02}\eta) + z_0. \tag{15}$$

This electron orbit has a cycloid trajectory in the x-y plane, as shown in Fig. 1(b). Although the electron trajectory is not closed for one laser period in general, when $\lambda_{01}/\lambda_{02}$ is an integer, it is closed and has $\lambda_{01}/\lambda_{02} - 1$ nodes, as shown in Figs. 2(j)–2(l). Equations (13)–(15) show that the electron moves counterclockwise when the observer is facing the oncoming electron. We say that this electron motion has positive helicity.

The phase term of Eqs. (11) and (12) can be expressed as

$$\begin{aligned} \psi = {}&\psi_0 + kg\eta - b_1\sin(k_{01}\eta - \phi) - b_2\sin(k_{02}\eta - \phi) \\ &+ b_{12}^{(-)}\sin(k_{01}\eta - k_{02}\eta), \end{aligned} \tag{16}$$

where

$$\psi_0 \equiv -k\{x_0\sin\theta\,\cos\phi + y_0\sin\theta\,\sin\phi + z_0(1+\cos\theta)\}, \tag{17}$$

$$g \equiv 1 - \beta_{12}(1+\cos\theta), \tag{18}$$

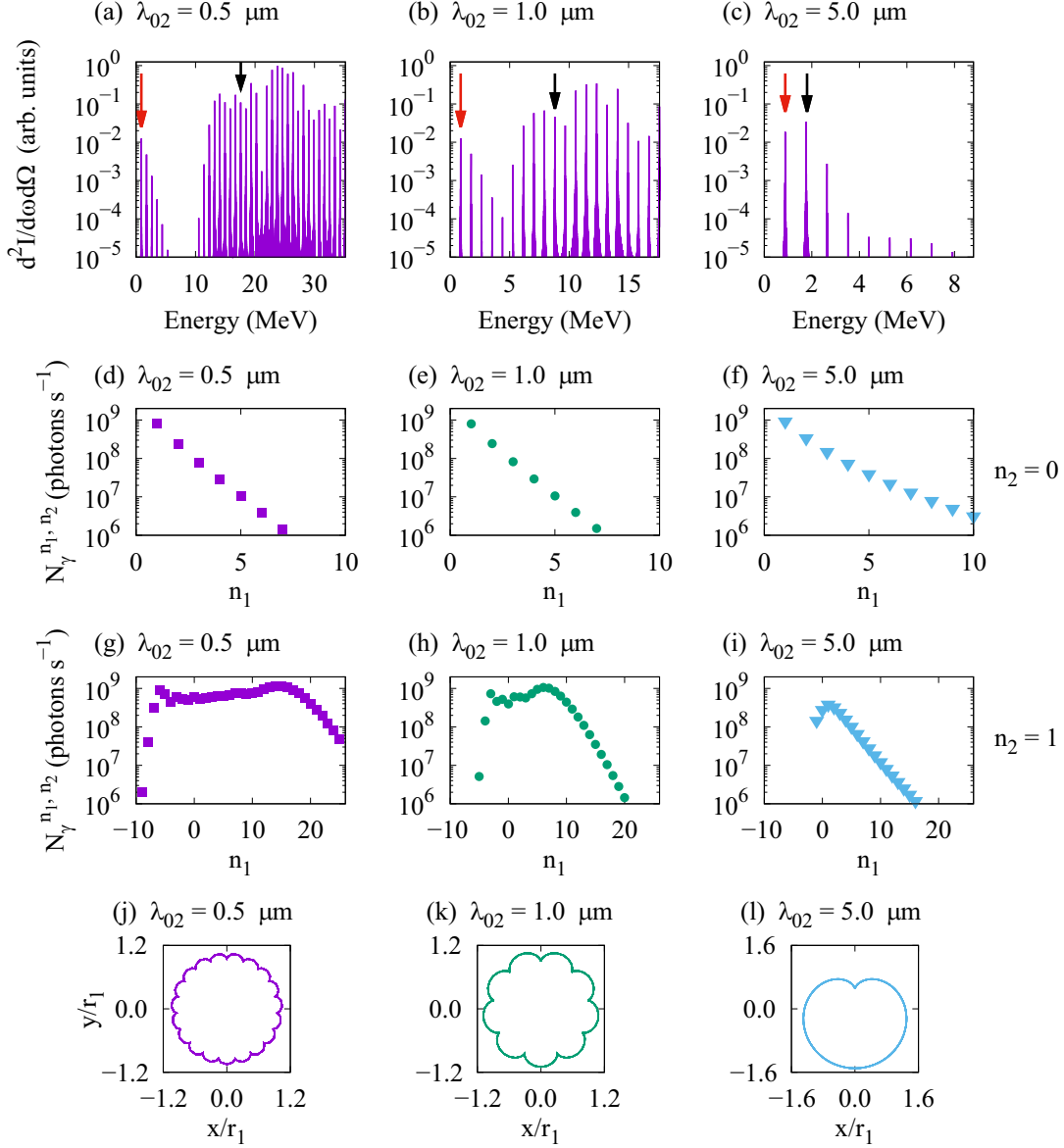$$b_{1,2} \equiv kr_{01,02}\sin\theta, \tag{19}$$

FIG. 2. (a)–(c) Energy spectra of gamma rays emitted by NITS with two circularly polarized laser beams at angle $\theta = 0.5/\gamma_0$ and calculated using Eq. (27). Red and black arrows show the fundamental scattered energy calculated using $\hbar\omega(n_1 = 1, n_2 = 0) = 4\gamma_0^2\hbar\omega_{01}/\{1 + \gamma_0^2\theta^2 + (a_{01}^2 + a_{02}^2)/2\}$ and $\hbar\omega(n_1 = 0, n_2 = 1) = 4\gamma_0^2\hbar\omega_{02}/\{1 + \gamma_0^2\theta^2 + (a_{01}^2 + a_{02}^2)/2\}$, respectively. (d)–(f) The number of gamma-ray photons integrated up to $\theta_c = 3/\gamma_0$ and calculated using Eq. (29). The harmonic number $n_2 = 0$. (g)–(i) Same as (d)–(f) but $n_2 = 1$. (j)–(l) Projection of normalized transverse electron trajectories inside two circularly polarized laser beams for $-5\lambda_{01} < \eta < 5\lambda_{01}$, as calculated using Eqs. (13)–(15). The calculation parameters are $\gamma_0 = 2000$, $\lambda_{01} = 10\ \mu m$, $a_{01} = 1$, $a_{02} = 1$, $N_{01} = 150$, and $N_e = 10^9$ electron s^{-1}. The wavelength of the second laser λ_{02} is indicated above each panel.

and

$$b_{12}^{(-)} \equiv kz_{012}^{(-)}(1 + \cos\theta). \tag{20}$$

The final expressions of Eqs. (11) and (12) are

$$
\begin{aligned}
E_\theta &= \sum_{n_1=-\infty}^{\infty}\sum_{n_2=-\infty}^{\infty}\sum_{s=-\infty}^{\infty} i\sqrt{\frac{e^2 k^2 \lambda_{01}^2 N_{01}^2}{32\pi^3\epsilon_0^2 c^2}}\frac{\sin(\overline{k}\eta_0)}{\overline{k}\eta_0}\frac{e^{i\psi_0 + ikR + i(n_1+n_2)\phi}}{R}\left\{\frac{1}{2}k_{01}r_{01}\cos\theta\left(J_{n_1+1,n_2} + J_{n_1-1,n_2}\right)\right. \\
&\quad + \frac{1}{2}k_{02}r_{02}\cos\theta\left(J_{n_1,n_2+1} + J_{n_1,n_2-1}\right) - \beta_{12}\sin\theta J_{n_1,n_2} + \frac{1}{2}(k_{01} - k_{02})z_{012}^{(-)}\sin\theta\left(J_{n_1+1,n_2-1} + J_{n_1-1,n_2+1}\right)\Big\} \\
&\equiv \sum_{n_1=-\infty}^{\infty}\sum_{n_2=-\infty}^{\infty} iC_\theta\frac{e^{i\psi_0 + ikR + i(n_1+n_2)\phi}}{R}
\end{aligned}
\tag{21}
$$

and

$$E_\phi = \sum_{n_1=-\infty}^{\infty} \sum_{n_2=-\infty}^{\infty} \sum_{s=-\infty}^{\infty} \sqrt{\frac{e^2 k^2 \lambda_{01}^2 N_{01}^2}{32\pi^3 \epsilon_0^2 c^2}} \frac{\sin(\overline{k}\eta_0)}{\overline{k}\eta_0} \frac{e^{i\psi_0+ikR+i(n_1+n_2)\phi}}{R} \left\{ \frac{1}{2} k_{01} r_{01} \left(J_{n_1+1,n_2} - J_{n_1-1,n_2} \right) \right.$$

$$\left. + \frac{1}{2} k_{02} r_{02} \left(J_{n_1,n_2+1} - J_{n_1,n_2-1} \right) \right\} \equiv \sum_{n_1=-\infty}^{\infty} \sum_{n_2=-\infty}^{\infty} C_\phi \frac{e^{i\psi_0+ikR+i(n_1+n_2)\phi}}{R}. \tag{22}$$

Here, n_1, n_2, and s are integers, $J_{n_1,n_2} \equiv J_{n_1+s}(b_1) J_{n_2-s}(b_2) J_s(b_{12}^{(-)})$, and $J_s()$ is the Bessel function of the first kind. Equations (21) and (22) have a peak at a wave number given by

$$\overline{k} \equiv kg - n_1 k_{01} - n_2 k_{02} = 0. \tag{23}$$

This equation indicates that n_1 and n_2 are the harmonic numbers of the initial laser energies as described in Eq. (28).

The photon is emitted into a narrow angle, $\theta \sim 1/\gamma_0$, around the z axis because of a relativistic effect. To show the phase structure in the transverse plane perpendicular to the z axis, we express the electric field in a Cartesian coordinate system as in a previous work [13,64]:

$$\mathbf{E} = \frac{E_x - iE_y}{\sqrt{2}} \mathbf{e}_+ + \frac{E_x + iE_y}{\sqrt{2}} \mathbf{e}_- + E_z \mathbf{e}_z$$

$$= \sum_{n_1=-\infty}^{\infty} \sum_{n_2=-\infty}^{\infty} \frac{e^{i\psi_0+ikR}}{R} \left\{ \frac{i(C_\theta \cos\theta - C_\phi)}{\sqrt{2}} e^{i(n_1+n_2-1)\phi} \mathbf{e}_+ + \frac{i(C_\theta \cos\theta + C_\phi)}{\sqrt{2}} e^{i(n_1+n_2+1)\phi} \mathbf{e}_- - iC_\theta \sin\theta^{i(n_1+n_2)\phi} \mathbf{e}_z \right\}. \tag{24}$$

Here, the electric field is expressed using complex orthogonal unit vectors $\mathbf{e}_\pm \equiv (\mathbf{e}_x \pm i\mathbf{e}_y)\sqrt{2}$. The helicities of the circularly polarized electric fields are positive and negative, respectively. For the positive helicity, the rotation of the electric field corresponds with the helicity of the electron. In the paraxial approximation ($\theta \ll 1$), the longitudinal electric-field component along the z axis of Eq. (24) is generally smaller than the transverse component. Equation (24) indicates that the electric field of the emitted photon is elliptically polarized in the transverse plane, which can be decomposed into circularly polarized components with positive and negative helicities. The positive helicity component has $+\hbar$ SAM and has a spiral phase term $\exp\{i(n_1+n_2-1)\phi\}$ with OAM equal to $(n_1+n_2-1)\hbar$. Conversely, the negative helicity component has $-\hbar$ SAM and has a spiral phase term $\exp\{i(n_1+n_2+1)\phi\}$ with OAM equal to $(n_1+n_2+1)\hbar$.

The energy of the scattered photon depends on the initial wavelength of the two laser beams, as shown in Eq. (28). However, the parameters kr_{01}, kr_{02}, and $kz_{012}^{(-)}$ in Eqs. (19) and (20) and $k\lambda_{01}$ in Eqs. (21) and (22), calculated using Eq. (23), are a function of $\lambda_{01}/\lambda_{02}$. Therefore, the electric fields of the emitted photons have the same form for different wavelengths, λ_{01} and λ_{02}, as long as $\lambda_{01}/\lambda_{02}$ is constant and $\overline{k} = 0$.

When the wavelength and the laser strength parameter of the two laser beams are the same ($\lambda_{01} = \lambda_{02}$ and $a_{01} = a_{02}$), the phase term and the inner products in Eqs. (11) and (12) reduce to the expressions for NITS using one laser [Eqs. (12), (15), and (16) in [13]].

Up to this point, we considered circular polarization with the same helicity. Here, we briefly describe when the two laser beams are circularly polarized but have opposite helicities. The normalized vector potential of the two laser beams is

defined as

$$\mathbf{a} = \left\{ \frac{a_{01}}{\sqrt{2}} \cos(k_{01}\eta) + \frac{a_{02}}{\sqrt{2}} \cos(k_{02}\eta) \right\} \mathbf{e}_x$$

$$+ \left\{ \frac{a_{01}}{\sqrt{2}} \sin(k_{01}\eta) - \frac{a_{02}}{\sqrt{2}} \sin(k_{02}\eta) \right\} \mathbf{e}_y. \tag{25}$$

The electron orbit also has a cycloid trajectory in the x-y plane. Although we do not show the detailed equations, the calculated electric fields include a spiral phase term, $\exp\{i(n_1-n_2)\phi\}$. The sign of the harmonic number n_2 is inverted because the helicity of the second laser is inverted, as shown in Eq. (25). The emitted photons have OAM equal to $(n_1-n_2-1)\hbar$ for positive helicity and $(n_1-n_2+1)\hbar$ for negative helicity.

C. Properties of the scattered radiation field

The degree of circular polarization of the emitted photon for the harmonic numbers n_1 and n_2 can be represented by the Stokes parameter, S_3/S_0, which is expressed as (Sec. 7.2 in [63])

$$\frac{S_3}{S_0} = \frac{-2C_\theta C_\phi \cos\theta}{C_\theta^2 \cos^2\theta + C_\phi^2}. \tag{26}$$

The radiation energy per unit angular frequency and the solid angle are expressed as (Sec. 14.5 in [63])

$$\frac{d^2 I}{d\omega \, d\Omega} = 2\epsilon_0 c R^2 |\mathbf{E}|^2$$

$$= 2\epsilon_0 c R^2 (|E_\theta|^2 + |E_\phi|^2). \tag{27}$$

Here, $d\Omega = d\phi \, d\theta \, \sin\theta$.

The spectrum given by Eq. (27) peaks at a specific photon energy, which can be calculated from Eq. (23). In the limit $\theta \ll 1$, it can be expressed as

$$\hbar\omega \simeq \frac{4\gamma_0^2(n_1\hbar\omega_{01} + n_2\hbar\omega_{02})}{1 + \gamma_0^2\theta^2 + (a_{01}^2 + a_{02}^2)/2}. \qquad (28)$$

Here, ω_{01} and ω_{02} are the angular frequencies of the two laser beams. Equation (28) gives the energy of the scattered photon via NITS of two laser beams and is common to any polarization combination including circular polarization with the opposite helicity, in which the sign of n_2 related to OAM is inverted. The harmonic numbers n_1 and n_2 can take arbitrary integers, including minus values, unless the scattered photon energy is less than or equal to zero [65].

For the harmonic numbers n_1 and n_2, the number of photons emitted per second for a scattering angle up to θ_c can be approximately calculated from Eq. (27) [13]:

$$
\begin{aligned}
N_\gamma^{n_1,n_2} &= \frac{N_e \Delta\omega}{\hbar\omega} \int_0^{2\pi} d\phi \int_0^{\theta_c} d\theta \, \sin\theta \frac{d^2 I^{n_1,n_2}}{d\omega \, d\Omega} \\
&= \frac{N_e}{\hbar(n_1 N_{01} + n_2 N_{02})} \int_0^{2\pi} d\phi \int_0^{\theta_c} d\theta \, \sin\theta \frac{d^2 I^{n_1,n_2}}{d\omega \, d\Omega} \\
&= \frac{N_e}{\hbar(n_1 + n_2 \lambda_{01}/\lambda_{02}) N_{01}} \\
&\quad \times \int_0^{2\pi} d\phi \int_0^{\theta_c} d\theta \, \sin\theta \frac{d^2 I^{n_1,n_2}}{d\omega \, d\Omega}. \qquad (29)
\end{aligned}
$$

Here, N_e is the number of electrons interacting with the two laser beams per second and $d^2 I^{n_1,n_2}/d\omega \, d\Omega$ is the radiation energy for the harmonic numbers n_1 and n_2. Here, we did the calculation by approximating $\bar{k} = 0$ and using the bandwidth of the scattered photons with a finite number of periods for the two laser beams, $\Delta\omega/\omega = 1/(n_1 N_{01} + n_2 N_{02})$. Equation (29) indicates that the number of photons is proportional to N_{01} and N_{02}.

III. RESULTS OF THE NUMERICAL CALCULATION FOR GAMMA-RAY VORTICES

A. Intensity of the scattered radiation field

High-power pulsed lasers, which can be used in the non-linear region, are available in the submicrometer to 10 μm range [25,54,66–68]. First, we show the properties of photons emitted for a combination of $\lambda_{01} = 10$ μm and $\lambda_{02} = 0.5$, 1, and 5 μm for circular polarization with the same helicity. For simplicity, we assume the laser strength parameters $a_{01} = a_{02} = 1$. We shall discuss the dependence of the laser strength parameter later.

Figures 2(a)–2(c) show the energy spectra of gamma-ray photons emitted at an angle of $\theta = 0.5/\gamma_0$ and calculated using Eq. (27). One can clearly see that the energy spectra have sharp peaks with an interval of $4\gamma_0^2 \hbar\omega_{01}/\{1 + \gamma_0^2\theta^2 + (a_{01}^2 + a_{02}^2)/2\}$, which is related to the photon energy of the longer wavelength laser. As shown in Fig. 2(c), when the second laser has a long wavelength close to that of the first one, the intensity decreases as the energy increases. On the other hand, when the second laser has a significantly shorter wavelength than the first one, one can see strong peaks around

the two fundamental energies, denoted by red and black arrows, and the intensity between these peaks is reduced, as shown in Figs. 2(a) and 2(b). This result is consistent with a previous work [59].

Figures 2(d)–2(i) show the number of photons for the harmonic numbers n_1 and n_2 integrated up to $\theta_c = 3/\gamma_0$ and calculated using Eq. (29). The results only for $n_2 = 0$ and 1 are displayed because the number of photons for $n_2 \leqslant -1$ and $n_2 \geqslant 2$ is relatively small. The number of photons for $n_2 = 0$ decreases as the harmonic number n_1 increases, as shown in Figs. 2(d)–2(f), which is consistent with NITS using one laser beam [13]. However, when $n_2 = 1$, the dependence of the number of photons on the harmonic number is much different. The number of photons is high in a wide range from negative values up to the harmonic number $n_1 \sim \lambda_{01}/\lambda_{02}$ and it reduces as the harmonic number increases, as shown in Figs. 2(g)–2(i).

The behavior of the intensity spectra has a strong correlation with the number of nodes of the cycloid motion. The transverse trajectories of an electron inside two circularly polarized laser beams are shown in Figs. 2(j)–2(l). Since the number of nodes of the cycloid motion, which is given by $\lambda_{01}/\lambda_{02} - 1$, increases, intense gamma rays are emitted up to the harmonic number $n_1 \sim \lambda_{01}/\lambda_{02}$ for $n_2 = 1$. We emphasize that the above result implies that the combination of long-wavelength and short-wavelength laser beams is advantageous for producing intense gamma-ray vortices with a large OAM.

B. Polarization and the spatial distribution of the radiation energy

In the following calculation, we show the numerical results for intense gamma rays calculated with the combination of long-wavelength ($\lambda_{01} = 10$ μm) and short-wavelength ($\lambda_{02} = 1$ μm) circularly polarized laser beams with the same helicity for $n_2 = 1$. The combined laser beam with strength parameters of $a_{01} = 1$ and $a_{02} = 1$, wavelengths of $\lambda_{01} = 10$ μm and $\lambda_{02} = 1$ μm, and numbers of periods of $N_{01} = 150$ and $N_{02} = 1500$ has an energy density of 7×10^4 J/cm^2 and a pulse width of 5 ps.

The degree of circular polarization of the emitted photons calculated for different values of the Stokes parameter [Eq. (26)] is shown in Figs. 3(a)–3(d). Stokes parameters of $S_3/S_0 = 1$ and -1 indicate 100% circular polarization with positive and negative helicities, respectively. The degree of circular polarization has different distributions depending on the harmonic number n_1. For most values of the Stokes parameter, there is circular polarization with positive helicity around the z axis, except for $n_1 = -2$ [Fig. 3(a)].

The spatial distributions of the radiation energy of the emitted gamma rays for each harmonic number are shown in Figs. 3(e)–3(h). The spatial distributions and OAM show a strong correlation. When the emitted photons have OAM, which satisfies $n_1 + n_2 - 1 \neq 0$ for positive helicity, one can clearly see annular shapes with zero intensity at the center axis, as shown in Figs. 3(f) and 3(h). Moreover, the diameter of the annular shapes increases as the OAM increases for $n_1 \geqslant 1$. These features are consistent with the characteristics of an optical vortex [3]. On the other hand, when the emitted photons do not carry OAM, which means $n_1 + n_2 - 1 = 0$ for positive helicity and $n_1 + n_2 + 1 = 0$ for negative helicity, the
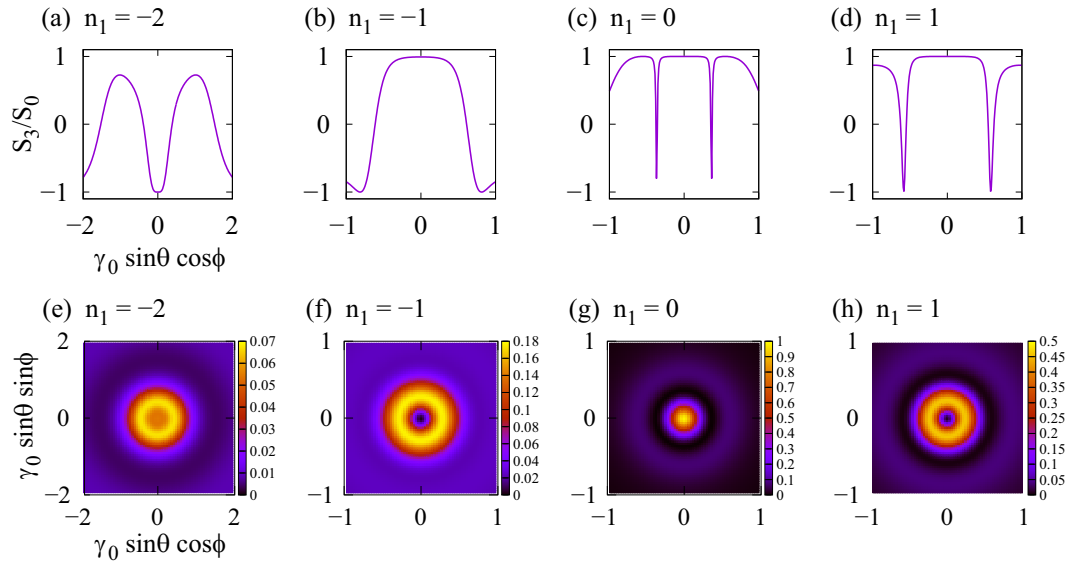
FIG. 3. (a)–(d) Line distributions of the Stokes parameter for gamma rays emitted by NITS for two circularly polarized laser beams with the same helicity. The Stokes parameter has cylindrical symmetry because Eq. (26) is not a function of ϕ. (e)–(h) Spatial distributions of the radiation energy of gamma rays calculated using Eq. (27). Each spatial distribution is normalized by the maximum value of $n_1 = 0$. The calculation parameters are $\gamma_0 = 2000$, $\lambda_{01} = 10 \ \mu$m, $\lambda_{02} = 1 \ \mu$m, $a_{01} = 1$, $a_{02} = 1$, and $n_2 = 1$. The harmonic number n_1 is indicated above the panels. Note that the scale for the horizontal axis in (a) and (e) is different from that in the other panels.

intensity at the center axis does not reduce to zero, as shown in Figs. 3(e) and 3(g).

C. OAM, the number of photons, and energy of the gamma-ray vortices

The OAM of the emitted gamma rays for $n_2 = 1$ increases as the harmonic number n_1 increases, since it is calculated using $n_1 + n_2 - 1$ for positive helicity, as shown in Fig. 4(a). Figure 4(b) shows the number of photons integrated up to θ_c, where this angle contains more than 90% of the circular polarization with positive helicity as calculated with the Stokes parameters of Figs. 3(a)–3(d). For NITS with a one-wavelength laser beam, the number of photons decreases as the harmonic number n_1 increases. However, for NITS with a two-wavelength laser beam, the number of photons

is a maximum at $n_1 = 5$, where the gamma rays have OAM equal to $5\hbar$, as shown in Fig. 4(b). This is because the solid angle containing more than 90% of the circular polarization with positive helicity is a maximum at $n_1 = 5$. The maximum energy of the gamma rays ($\theta = 0$) is shown in Fig. 4(c). The fundamental photon energies for the laser beams with $\lambda_{01} = 10 \ \mu$m and $\lambda_{02} = 1 \ \mu$m are 1 and 10 MeV, respectively. The energy of the gamma rays increases by 1 MeV as the harmonic number n_1 increases by 1. Each OAM state is well separated by energy.

IV. DISCUSSION

In this section, we discuss the optimum laser parameters to generate intense gamma-ray vortices with a specific OAM. We calculated the number of photons for different wavelengths
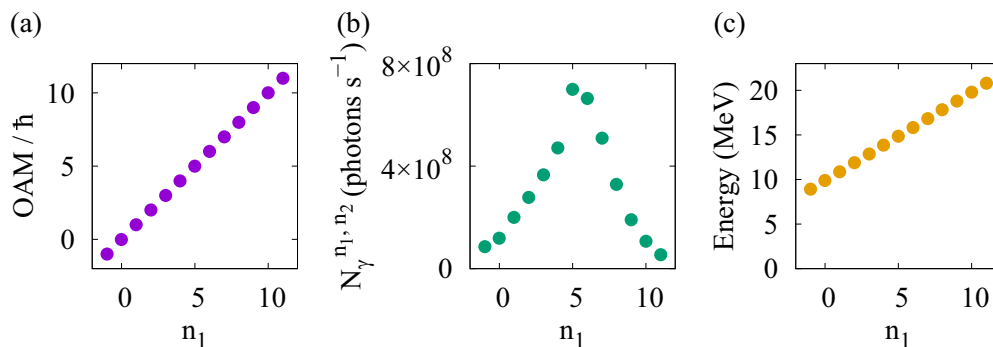

FIG. 4. (a) OAM of gamma-ray vortices calculated using $n_1 + n_2 - 1$ for positive helicity as a function of harmonic number n_1. (b) The number of gamma-ray photons integrated for a solid angle up to θ_c, which contains more than 90% of the circular polarization with positive helicity. (c) Maximum energy of gamma-ray vortices ($\theta = 0$) calculated using Eq. (28). The calculation parameters are $\gamma_0 = 2000$, $\lambda_{01} = 10 \ \mu$m, $\lambda_{02} = 1 \ \mu$m, $a_{01} = 1$, $a_{02} = 1$, $N_{01} = 150$, $N_{02} = 1500$, $n_2 = 1$, and $N_e = 10^9$ electron s^{-1}.
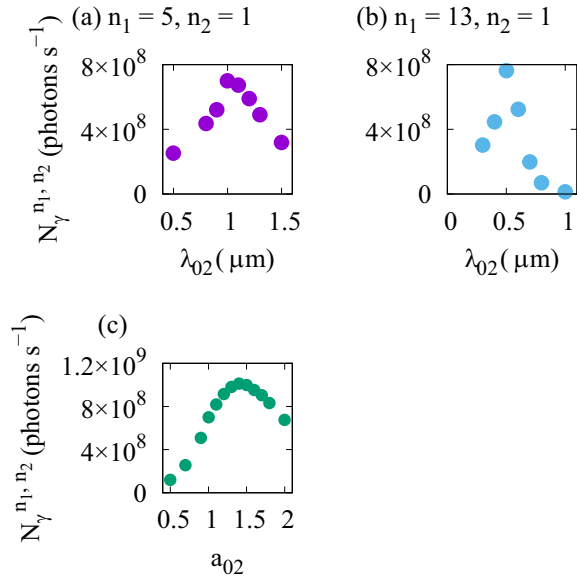
FIG. 5. Number of gamma-ray photons integrated over the solid angle up to θ_c, which contains more than 90% of the circular polarization with positive helicity. The calculation parameters are $\gamma_0 = 2000$, $\lambda_{01} = 10 \mu$m, $a_{01} = 1$, $N_{01} = 150$, $n_2 = 1$, and $N_e = 10^9$ electron s^{-1}. The other parameters are (a) $a_{02} = 1$ and $n_1 = 5$, (b) $a_{02} = 1$ and $n_1 = 13$, and (c) $\lambda_{02} = 1 \mu$m and $n_1 = 5$.

of the second laser and for harmonic numbers $n_1 = 5$ and $n_2 = 1$. This gives the most intense gamma-ray vortex, which has OAM equal to $5\hbar$ when $\lambda_{01} = 10 \mu$m and $\lambda_{02} = 1 \mu$m. As λ_{02} becomes longer, the diameter of the annular shape gradually increases. On the other hand, the maximum angles containing more than 90% of the circular polarization with positive helicity increase until $\lambda_{02} = 1.0 \mu$m as λ_{02} becomes longer, and they decrease for $\lambda_{02} > 1.0 \mu$m. The number of photons integrated in the solid angle up to θ_c, which contains more than 90% of the circular polarization with positive helicity, is a maximum at $\lambda_{02} = 1 \mu$m because of these effects, as shown in Fig. 5(a).

We calculated the number of photons for gamma-ray vortices with harmonic numbers $n_1 = 13$ and $n_2 = 1$ and with OAM equal to $13\hbar$ using a similar calculation method for $0.3 \leqslant \lambda_{02} \leqslant 1.0 \mu$m. As shown in Fig. 5(b), the number of photons is a maximum at $\lambda_{02} = 0.5 \mu$m. We should emphasize that there is an appropriate combination of wavelengths to produce gamma-ray vortices with a specific OAM. When the first laser beam has a wavelength of 10 μm, a second 1 μm laser beam can produce intense gamma-ray vortices with an OAM equal to $5\hbar$. To produce gamma-ray vortices with a larger OAM, such as $13\hbar$, we can use a second laser beam with a wavelength of 0.5 μm.

The number of gamma-ray vortex photons generally increases as the laser strength increases, and it saturates for $a_0 > 2$ for NITS using one laser beam [64]. Figure 5(c) shows the number of photons for more than 90% of the circular polarization with positive helicity for different laser strengths of the second laser and for harmonic numbers $n_1 = 5$ and $n_2 = 1$. As a_{02} increases, the diameter of the annular shape gradually increases. On the other hand, the maximum angles

containing more than 90% of the circular polarization with positive helicity increase as a_{02} increases until $a_{02} = 1.0$, and they shrink for $a_{02} > 1.0$. The number of photons is a maximum at $a_{02} = 1.4$ when $a_{01} = 1.0$, as shown in Fig. 5(c).

The number of photons rapidly decreases as the harmonic number n_2 increases when both a_{01} and a_{02} are smaller than the unity. As a result, plateaus appearing in Figs. 2(g) and 2(h) disappear in this condition. Therefore, intense laser beams of $a_0 \sim 1$ are indeed necessary for generating gamma-ray vortices carrying a large OAM.

The generation of optical vortex photons by NITS is physically similar to undulator radiation, as discussed in the literature [38,44,69–71]. The laser strength and the wavelength of the laser are like the undulator strength parameter, K, and the period length of the undulator, respectively. The generation of optical vortices from helical undulators was theoretically proposed [72] and later experimentally verified [73–76]. The phase term, $\exp\{i(m-1)\phi\}$, can be seen in the complex amplitude of an emitted photon. An annular intensity distribution was observed only for the higher harmonics ($m \geqslant 2$).

An electron with a cycloid motion can be achieved by a two-frequency undulator. Although linear polarization has been considered in the previous works [65,77–81], a two-frequency helical undulator may be realized with, for example, a superconducting bifilar solenoid (Sec. 14-7-1 in [82]). Such a device would emit photons at ultraviolet and x-ray wavelengths. They would have a spiral phase term $\exp\{i(n_1 + n_2 \pm 1)\phi\}$ and a large OAM. Although we treated a spiral phase term of radiation emitted from an single electron in this work, an effective electron beam inside an accelerator device has the finite emittance. The emittance of an electron beam affects the detection of a helical wave front of an optical vortex. As discussed in the references of [73,75], interference fringes are smeared out by the emittance.

NITS has been discussed as a candidate for radiation processes in astrophysical environments, e.g., pulsars [39–41]. In our other work, we have theoretically demonstrated that optical vortices are naturally produced by NITS in astrophysical situations where electrons interact with intense electromagnetic waves at arbitrary angles [64]. Intense electromagnetic waves are thought to exist near pulsars [83] and may be emitted during gamma-ray bursts [84] at various frequencies from radio to infrared. In such environments, intense electromagnetic waves with various wavelengths and high-energy electrons likely coexist, and high-energy photons with a large OAM would be produced via NITS.

Thomson scattering, which is considered in this paper, occurs when the energy of the scattered photon is much smaller than the initial electron energy, i.e., $\hbar\omega \ll \gamma_0 m_e c^2$, as described in [44], where $m_e c^2$ is the electron rest energy. Using Eq. (28), we can write

$$\gamma_0 \ll \frac{1 + \gamma_0^2 \theta^2 + (a_{01}^2 + a_{02}^2)/2}{4(n_1 \hbar\omega_{01} + n_2 \hbar\omega_{02})} m_e c^2. \tag{30}$$

When $\lambda_{01} = 10 \mu$m, $\lambda_{02} = 1 \mu$m, $a_{01} = a_{02} = 1$, $n_1 = 5$, $n_2 = 1$, and $\theta = 0$, Eq. (30) gives $\gamma_0 \ll 1.4 \times 10^5$ and $\hbar\omega \ll 70$ GeV. Therefore, our result is valid for gamma-ray vortex generation in the MeV energy range up to ~ 1 GeV.

V. CONCLUSIONS

In this paper, NITS using a two-wavelength laser beam was investigated. We found that an electron inside two circularly polarized laser fields follows a cycloid trajectory in the transverse plane, the electric fields emitted from such an electron have a spiral phase term $\exp\{i(n_1 + n_2 \pm 1)\phi\}$, and the electron has OAM equal to $(n_1 + n_2 \pm 1)\hbar$ in addition to SAM. Spatial distributions of the radiation energy of emitted photons have annular shapes when OAM $\neq 0$, which is typical of an optical vortex. In NITS with a one-wavelength laser, an extremely high-power laser with $a_0 > 10$ is required to produce gamma-ray vortices with large OAM [64]. However, NITS with a two-wavelength laser beam can produce intense gamma-ray vortices with a large OAM of $\sim 10\hbar$ using two less intense laser beams with $a_0 \sim 1$. Each OAM state of the gamma-ray vortices characterized by harmonic numbers is well separated by energy. This may be beneficial for applications. The theory developed could be applied to a two-frequency helical undulator, which would enable the generation of ultraviolet and x-ray vortices. Moreover, this radiation process may play an important role in the astrophysical environments.

to the verification of the analytic calculations and the discussions.

APPENDIX A: SPATIAL DISTRIBUTION OF RADIATION ENERGY WITH LINEAR POLARIZATION

Here, we derive the equations when both laser beams have linear polarization to calculate the spatial distribution of the radiation energy, which is not described in a previous work [59]. We assume that the two laser beams are linearly polarized along the x axis [$\delta_{01} = \delta_{02} = 1$ in Eqs. (3)–(5)]. The phase term of Eqs. (11) and (12) is

$$
\begin{aligned}
\psi = {} & \psi_0 + kg\eta - b_1' \sin(k_{01}\eta) - b_2' \sin(2k_{01}\eta) - b_3' \sin(k_{02}\eta) \\
& - b_4' \sin(2k_{02}\eta) + b_{12}^{(-)} \sin(k_{01}\eta - k_{02}\eta) \\
& + b_{12}^{(+)} \sin(k_{01}\eta + k_{02}\eta),
\end{aligned} \tag{A1}
$$

where

$$
b_1' \equiv \sqrt{2} k r_{01} \sin\theta \, \cos\phi, \tag{A2}
$$

$$
b_2' \equiv -k z_{01}(1 + \cos\theta), \tag{A3}
$$

$$
b_3' \equiv \sqrt{2} k r_{02} \sin\theta \, \cos\phi, \tag{A4}
$$

$$
b_4' \equiv -k z_{02}(1 + \cos\theta), \tag{A5}
$$

and

$$
b_{12}^{(+)} \equiv k z_{012}^{(+)}(1 + \cos\theta). \tag{A6}
$$

The electric field for linear polarization can be expressed as

$$
\begin{aligned}
E_\theta = {} & \sum_{n_1=-\infty}^{\infty} \sum_{n_2=-\infty}^{\infty} \sum_{m=-\infty}^{\infty} \sum_{s=-\infty}^{\infty} i \sqrt{\frac{e^2 k^2 \lambda_{01}^2 N_{01}^2}{32\pi^3 \epsilon_0^2 c^2}} \frac{\sin(\bar{k}\eta_0)}{\bar{k}\eta_0} \frac{e^{i\psi_0 + ikR}}{R} \left\{ \frac{1}{\sqrt{2}} k_{01} r_{01} \cos\theta \, \cos\phi \left(J''_{n_1+1,n_2} + J''_{n_1-1,n_2} \right) + \frac{1}{\sqrt{2}} k_{02} r_{02} \right. \\
& \times \cos\theta \, \cos\phi \left(J''_{n_1,n_2+1} + J''_{n_1,n_2-1} \right) - \beta_{12} \sin\theta \, J''_{n_1,n_2} + k_{01} z_{01} \sin\theta \left(J''_{n_1+2,n_2} + J''_{n_1-2,n_2} \right) + k_{02} z_{02} \sin\theta \left(J''_{n_1,n_2+2} + J''_{n_1,n_2-2} \right) \\
& \left. + \frac{1}{2}(k_{01} - k_{02}) z_{012}^{(-)} \sin\theta \left(J''_{n_1+1,n_2-1} + J''_{n_1-1,n_2+1} \right) + \frac{1}{2}(k_{01} + k_{02}) z_{012}^{(+)} \sin\theta \left(J''_{n_1+1,n_2+1} + J''_{n_1-1,n_2-1} \right) \right\}
\end{aligned} \tag{A7}
$$

and

$$
\begin{aligned}
E_\phi = {} & \sum_{n_1=-\infty}^{\infty} \sum_{n_2=-\infty}^{\infty} \sum_{m=-\infty}^{\infty} \sum_{s=-\infty}^{\infty} i \sqrt{\frac{e^2 k^2 \lambda_{01}^2 N_{01}^2}{32\pi^3 \epsilon_0^2 c^2}} \frac{\sin(\bar{k}\eta_0)}{\bar{k}\eta_0} \frac{e^{i\psi_0 + ikR}}{R} \\
& \times \left\{ -\frac{1}{\sqrt{2}} k_{01} r_{01} \sin\phi \left(J''_{n_1+1,n_2} + J''_{n_1-1,n_2} \right) - \frac{1}{\sqrt{2}} k_{02} r_{02} \sin\phi \left(J''_{n_1,n_2+1} + J''_{n_1,n_2-1} \right) \right\}.
\end{aligned} \tag{A8}
$$

Here, m is an integer, $J''_{n_1,n_2} \equiv J_{n_1+m+s}(b_1', b_2')$ $J_{n_2-m+s}(b_3', b_4') J_m(b_{12}^{(-)}) J_s(b_{12}^{(+)})$ and $J_m(x_t, y_t)$ is the two-variable (x_t, y_t) generalized Bessel function of the first kind [85–87], defined by the series expansion:

$$
J_m(x_t, y_t) = \sum_{r=-\infty}^{\infty} J_{m-2r}(x_t) J_r(y_t). \tag{A9}
$$

Its integral representation can be expressed as [86]

$$
J_m(x_t, y_t) = \frac{1}{\pi} \int_0^\pi d\Phi \, \cos\{m\Phi - x_t \sin\Phi - y_t \sin(2\Phi)\}. \tag{A10}
$$

From Eqs. (A7) and (A8), the spiral phase term appearing with circular polarization is not seen for linear polarization.
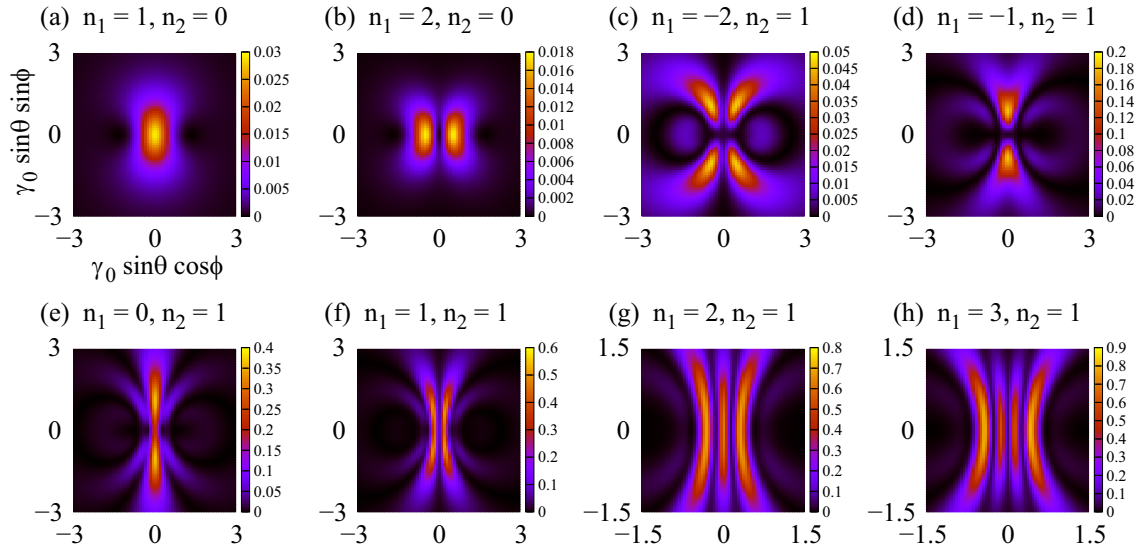
FIG. 6. Spatial distribution of the radiation energy of gamma rays emitted by NITS with two linearly polarized laser beams, calculated from Eq. (27). Each spatial distribution is normalized by the maximum values of $n_1 = 5$ and $n_2 = 1$. The calculation parameters are $\gamma_0 = 2000$, $\lambda_{01} = 10\,\mu\text{m}$, $\lambda_{02} = 1\,\mu\text{m}$, $a_{01} = 1$, and $a_{02} = 1$. The harmonic numbers n_1 and n_2 are indicated above each panel. Note that the scales of the horizontal axes in (g) and (h) are different from those of the other panels.

However, when the polarization of one laser beam is circular and the other is linear [$\delta_{01} = 0$ and $\delta_{02} = 1$ in Eqs. (3)–(5)], the calculated electric fields include the spiral phase term $\exp(in_1\phi)$. Therefore, the higher harmonic photons in the first laser beam have OAM.

The radiation energy per unit angular frequency and the solid angle can be calculated using Eq. (27). The number of photons integrated up to $\theta_c = 3/\gamma_0$ almost has the same trend as shown in Figs. 2(d)–2(i). The spatial distributions of the radiation energy of intense gamma rays are shown in Fig. 6. The spatial distributions for $n_2 = 0$ in Figs. 6(a) and 6(b) correspond to those of NITS with one laser beam [45]. The intensity of the even harmonics vanishes at the center axis ($\theta = 0$), but the odd harmonics have a peak at the center axis. Any particular harmonic n_1 has n_1 peaks along the direction of polarization. On the other hand, the distributions of the radiation energy for $n_2 = 1$ are complicated. When $n_1 + n_2$ is greater than or equal to 1, the intensity of the even harmonics vanishes at the center axis, but the odd harmonics have a peak, and any particular harmonic $n_1 + n_2$ has $n_1 + n_2$ peaks along the direction of polarization, as shown in Figs. 6(e)–6(h). When $n_1 + n_2$ is smaller than 1, the intensity vanishes at the center axis, and the distribution varies with $n_1 + n_2$, as shown in Figs. 6(c) and 6(d).

APPENDIX B: INITIAL PHASE OF THE VECTOR POTENTIAL OF THE TWO LASER BEAMS

In the main text, we assumed that the initial phase of the two laser beams at $\eta = 0$ was the same, as shown in Eq. (1). The vector potential of the two laser beams, including the initial phases ϕ_{01} and ϕ_{02}, can be expressed as

$$
\mathbf{a} = \left\{ \frac{a_{01}}{\sqrt{2}}\sqrt{1+\delta_{01}}\cos(k_{01}\eta + \phi_{01}) \right.
$$
$$
\left. + \frac{a_{02}}{\sqrt{2}}\sqrt{1+\delta_{02}}\cos(k_{02}\eta + \phi_{02}) \right\}\mathbf{e}_x
$$
$$
+ \left\{ \frac{a_{01}}{\sqrt{2}}\sqrt{1-\delta_{01}}\sin(k_{01}\eta + \phi_{01}) \right.
$$
$$
\left. + \frac{a_{02}}{\sqrt{2}}\sqrt{1-\delta_{02}}\sin(k_{02}\eta + \phi_{02}) \right\}\mathbf{e}_y. \quad \text{(B1)}
$$

The initial phase shifts of the incident laser beams, ϕ_{01} and ϕ_{02}, contribute only to the constant phase shifts of the scattered radiation field by adding the phase term $\exp(-in_1\phi_{01} - in_2\phi_{02})$ to Eqs. (21) and (22). They can be incorporated into the constant phase term, ψ_0.

[1] I. V. Basistiy, M. S. Soskin, and M. V. Vasnetsov, Optical wavefront dislocations and their properties, Opt. Commun. **119**, 604 (1995).

[2] L. Allen, M. W. Beijersbergen, R. J. C. Spreeuw, and J. P. Woerdman, Orbital angular momentum of light and the transformation of Laguerre-Gaussian laser modes, Phys. Rev. A **45**, 8185 (1992).

[3] L. Allen, M. J. Padgett, and M. Babiker, IV The orbital angular momentum of light, Prog. Opt. **39**, 291 (1999).

[4] G. Molina-Terriza, J. P. Torres, and L. Torner, Twisted photons, Nat. Phys. **3**, 305 (2007).

[5] A. M. Yao and M. J. Padgett, Orbital angular momentum: origins, behavior and applications, Adv. Opt. Photon. **3**, 161 (2011).

[6] A. Picón, J. Mompart, J. R. V. de Aldana, L. Plaja, G. F. Calvo, and L. Roso, Photoionization with orbital angular momentum beams, Opt. Express **18**, 3660 (2010).

[7] M. van Veenendaal and I. McNulty, Prediction of Strong Dichroism Induced by X Rays Carrying Orbital Momentum, Phys. Rev. Lett. **98**, 157401 (2007).

[8] S. Stock, A. Surzhykov, S. Fritzsche, and D. Seipt, Compton scattering of twisted light: Angular distribution and polarization of scattered photons, Phys. Rev. A **92**, 013401 (2015).

[9] T. Maruyama, T. Hayakawa, and T. Kajino, Compton scattering of gamma-ray vortex with Laguerre Gaussian wave function, arXiv:1710.09369.

[10] J. A. Sherwin, Theoretical study of the double Compton effect with twisted photons, Phys. Rev. A **95**, 052101 (2017).

[11] J. A. Sherwin, Compton scattering of Bessel light with large recoil parameter, Phys. Rev. A **96**, 062120 (2017).

[12] A. Afanasev, V. G. Serbo, and M. Solyanik, Radiative capture of cold neutrons by protons and deuteron photodisintegration with twisted beams, J. Phys. G: Nucl. Part. Phys. **45**, 055102 (2018).

[13] Y. Taira, T. Hayakawa, and M. Katoh, Gamma-ray vortices from nonlinear inverse Thomson scattering of circularly polarized light, Sci. Rep. **7**, 5018 (2017).

[14] A. G. Peele, P. J. McMahon, D. Paterson, C. Q. Tran, A. P. Mancuso, K. A. Nugent, J. P. Hayes, E. Harvey, B. Lai, and I. McNulty, Observation of an x-ray vortex, Opt. Lett. **27**, 1752 (2002).

[15] A. G. Peele and K. A. Nugent, X-ray vortex beams: A theoretical analysis, Opt. Express **11**, 2315 (2003).

[16] A. G. Peele, K. A. Nugent, A. P. Mancuso, D. Paterson, I. McNulty, and J. P. Hayes, X-ray phase vortices: theory and experiment, J. Opt. Soc. Am. A **21**, 1575 (2004).

[17] Y. Kohmura, K. Sawada, M. Taguchi, T. Ishikawa, T. Ohigashi, and Y. Suzuki, Formation of x-ray vortex dipoles using a single diffraction pattern and direct phase measurement using interferometry, Appl. Phys. Lett. **94**, 101112 (2009).

[18] Y. Takahashi, A. Suzuki, S. Furutaku, K. Yamauchi, Y. Kohmura, and T. Ishikawa, Bragg x-ray ptychography of a silicon crystal: Visualization of the dislocation strain field and the production of a vortex beam, Phys. Rev. B **87**, 121201 (2013).

[19] J. Vila-Comamala, A. Sakdinawat, and M. Guizar-Sicairos, Characterization of x-ray phase vortices by ptychographic coherent diffractive imaging, Opt. Lett. **39**, 5281 (2014).

[20] K. S. Morgan, T. C. Petersen, M. Donnelley, N. Farrow, D. W. Parsons, and D. M. Paganin, Capturing and visualizing transient x-ray wavefront topological features by single-grid phase imaging, Opt. Express **24**, 24435 (2016).

[21] U. D. Jentschura and V. G. Serbo, Generation of High-energy Photons with Large Orbital Angular Momentum by Compton Backscattering, Phys. Rev. Lett. **106**, 013001 (2011).

[22] V. Petrillo, G. Dattoli, I. Drebot, and F. Nguyen, Compton Scattered X-gamma Rays with Orbital Momentum, Phys. Rev. Lett. **117**, 123903 (2016).

[23] C. Liu, B. Shen, X. Zhang, Y. Shi, L. Ji, W. Wang, L. Yi, L. Zhang, T. Xu, Z. Pei, and Z. Xu, Generation of gamma-ray beam with orbital angular momentum in the QED regime, Phys. Plasmas **23**, 093120 (2016).

[24] M. Katoh, M. Fujimoto, H. Kawaguchi, K. Tsuchiya, K. Ohmi, T. Kaneyasu, Y. Taira, M. Hosaka, A. Mochihashi, and Y.

Takashima, Angular Momentum of Twisted Radiation from an Electron in Spiral Motion, Phys. Rev. Lett. **118**, 094801 (2017).

[25] Y. Sakai, I. Pogorelsky, O. Williams, F. O'Shea, S. Barber, I. Gadjev, J. Duris, P. Musumeci, M. Fedurin, A. Korostyshevsky, B. Malone, C. Swinson, G. Stenby, K. Kusche, M. Babzien, M. Montemagno, P. Jacob, Z. Zhong, M. Polyanskiy, V. Yakimenko, and J. Rosenzweig, Observation of redshifting and harmonic radiation in inverse Compton scattering, Phys. Rev. ST Accel. Beams **18**, 060702 (2015).

[26] H. Toyokawa, Transmission computerized tomography with a high-energy and quasi-monochromatic photon beam, Nucl. Instrum. Methods, Phys. Res. A **545**, 469 (2005).

[27] H. R. Weller, M. W. Ahmed, H. Gao, W. Tornow, Y. K. Wu, M. Gai, and R. Miskimen, Research opportunities at the upgraded HIγS facility, Prog. Part. Nucl. Phys. **62**, 257 (2009).

[28] D. B. Gustavson, J. J. Murray, T. J. Phillips, R. F. Schwitters, C. K. Sinclair, J. R. Johnson, R. Prepost, and D. E. Wiser, A backscattered laser polarimeter e+e− storage rings, Nucl. Instrum. Methods **165**, 177 (1979).

[29] R. Klein, T. Mayer, P. Kuske, R. Thornagel, and G. Ulm, Beam diagnostics at the BESSY I electron storage ring with Compton backscattered laser photons: measurement of the electron energy and related quantities, Nucl. Instrum. Methods, Phys. Res. A **384**, 293 (1997).

[30] T. Suehara, M. Oroku, T. Yamanaka, H. Yoda, T. Nakamura, Y. Kamiya, Y. Honda, T. Kume, T. Tauchi, T. Sanuki, and S. Komamiya, A nanometer beam size monitor for ATF2, Nucl. Instrum. Methods, Phys. Res. A **616**, 1 (2010).

[31] Y. Taira, H. Toyokawa, R. Kuroda, N. Yamamoto, M. Adachi, S. Tanaka, and M. Katoh, Photon-induced positron annihilation lifetime spectroscopy using ultrashort laser-Compton-scattered gamma-ray pulses, Rev. Sci. Instrum. **84**, 053305 (2013).

[32] T. Ishibashi, Y. Tomota, S. Sugaya, H. Toyokawa, T. Hirade, Z. Horita, and H. Suzuki, Bulky averaged microscopic information for ecap-processed Cu using accelerator-based gamma-ray-induced positron annihilation spectroscopy and neutron diffraction, Mater. Trans. **54**, 1562 (2013).

[33] F. Hori, Y. Ueno, K. Ishii, T. Ishiyama, A. Iwase, S. Miyamoto, and T. Terasawa, Positron annihilation Doppler broadening measurement for bulk amorphous alloy by using high energy positron generated from LCS gamma-ray at New SUBARU, J. Phys.: Conf. Ser. **674**, 012025 (2016).

[34] M. Fukuda, T. Aoki, K. Dobashi, T. Hirose, T. Iimura, Y. Kurihara, T. Okugi, T. Omori, I. Sakai, J. Urakawa, and M. Washio, Polarimetry of Short-pulse Gamma Rays Produced Through Inverse Compton Scattering of Circularly Polarized Laser Beams, Phys. Rev. Lett. **91**, 164801 (2003).

[35] Vachaspati, Harmonics in the scattering of light by free electrons, Phys. Rev. **128**, 664 (1962).

[36] L. S. Brown and T. W. B. Kibble, Interaction of intense laser beams with electrons, Phys. Rev. **133**, A705 (1964).

[37] I. I. Goldman, Intensity effects in Compton scattering, Phys. Lett. **8**, 103 (1964).

[38] E. S. Sarachik and G. T. Schappert, Classical theory of the scattering of intense laser radiation by free electrons, Phys. Rev. D **1**, 2738 (1970).

[39] J. E. Gunn and J. P. Ostriker, On the motion and radiation of charged particles in strong electromagnetic waves. I. Motion in plane and spherical waves, Astrophys. J. **165**, 523 (1971).

[40] P. Stewart, Non-linear Compton and inverse Compton effect, Astrophys. Space Sci. **18**, 377 (1972).

[41] J. Arons, Nonlinear inverse Comption radiation and the circular polarization of diffuse radiation from the crab nebula, Astrophys. J. **177**, 395 (1972).

[42] A. K. Puntajer and C. Leubner, Classical versus semiclassical predictions for harmonic generation in laser-free electron scattering under experimentally realizable conditions, J. Appl. Phys. **67**, 1606 (1990).

[43] E. Esarey and P. Sprangle, Generation of stimulated backscattered harmonic radiation from intense-laser interactions with beams and plasmas, Phys. Rev. A **45**, 5872 (1992).

[44] E. Esarey, S. K. Ride, and P. Sprangle, Nonlinear Thomson scattering of intense laser pulses from beams and plasmas, Phys. Rev. E **48**, 3003 (1993).

[45] S. K. Ride, E. Esarey, and M. Baine, Thomson scattering of intense lasers from electron beams at arbitrary interaction angles, Phys. Rev. E **52**, 5425 (1995).

[46] F. V. Hartemann and A. K. Kerman, Classical Theory of Nonlinear Compton Scattering, Phys. Rev. Lett. **76**, 624 (1996).

[47] F. V. Hartemann, A. L. Troha, H. A. Baldis, A. Gupta, A. K. Kerman, E. C. Landahl Jr., N. C. Luhmann, and J. R. Van Meter, High-intensity scattering processes of relativistic electrons in vacuum and their relevance to high-energy astrophysics, Astrophys. J., Suppl. Ser. **127**, 347 (2000).

[48] Y. Y. Lau, F. He, D. P. Umstadter, and R. Kowalczyk, Nonlinear Thomson scattering: A tutorial, Phys. Plasmas **10**, 2155 (2003).

[49] L. Dongguo, K. Yokoya, T. Hirose, and R. Hamatsu, Transition probability and polarization of final photons in nonlinear Compton scattering for linearly polarized laser, Jpn. J. Appl. Phys. **42**, 5376 (2003).

[50] G. A. Krafft and G. Priebe, Compton sources of electromagnetic radiation, Rev. Accel. Sci. Technol. **03**, 147 (2010).

[51] C. Bula, K. T. McDonald, E. J. Prebys, C. Bamber, S. Boege, T. Kotseroglou, A. C. Melissinos, D. D. Meyerhofer, W. Ragg, D. L. Burke, R. C. Field, G. Horton-Smith, A. C. Odian, J. E. Spencer, D. Walz, S. C. Berridge, W. M. Bugg, K. Shmakov, and A. W. Weidemann, Observation of Nonlinear Effects in Compton Scattering, Phys. Rev. Lett. **76**, 3116 (1996).

[52] D. L. Burke, R. C. Field, G. Horton-Smith, J. E. Spencer, D. Walz, S. C. Berridge, W. M. Bugg, K. Shmakov, A. W. Weidemann, C. Bula, K. T. McDonald, E. J. Prebys, C. Bamber, S. J. Boege, T. Koffas, T. Kotseroglou, A. C. Melissinos, D. D. Meyerhofer, D. A. Reis, and W. Ragg, Positron Production in Multiphoton Light-by-light Scattering, Phys. Rev. Lett. **79**, 1626 (1997).

[53] M. Babzien, I. Ben-Zvi, K. Kusche, I. V. Pavlishin, I. V. Pogorelsky, D. P. Siddons, V. Yakimenko, D. Cline, F. Zhou, T. Hirose, Y. Kamiya, T. Kumita, J. Urakawa, and K. Yokoya, Observation of the Second Harmonic in Thomson Scattering from Relativistic Electrons, Phys. Rev. Lett. **96**, 054802 (2006).

[54] Y. Sakai, I. Gadjev, P. Hoang, N. Majernik, A. Nause, A. Fukasawa, O. Williams, M. Fedurin, B. Malone, C. Swinson, K. Kusche, M. Polyanskiy, M. Babzien, M. Montemagno, Z. Zhong, P. Siddons, I. Pogorelsky, V. Yakimenko, T. Kumita, Y. Kamiya, and J. B. Rosenzweig, Single shot, double differential spectral measurements of inverse Compton scattering in the nonlinear regime, Phys. Rev. Accel. Beams **20**, 060701 (2017).

[55] G. Sarri, D. J. Corvan, W. Schumaker, J. M. Cole, A. Di Piazza, H. Ahmed, C. Harvey, C. H. Keitel, K. Krushelnick, S. P. D. Mangles, Z. Najmudin, D. Symes, A. G. R. Thomas, M. Yeung, Z. Zhao, and M. Zepf, Ultrahigh Brilliance Multi-MeV γ-ray Beams from Nonlinear Relativistic Thomson Scattering, Phys. Rev. Lett. **113**, 224801 (2014).

[56] K. Khrennikov, J. Wenz, A. Buck, J. Xu, M. Heigoldt, L. Veisz, and S. Karsch, Tunable All-optical Quasimonochromatic Thomson X-ray Source in the Nonlinear Regime, Phys. Rev. Lett. **114**, 195003 (2015).

[57] W. Yan, C. Fruhling, G. Golovin, D. Haden, J. Luo, P. Zhang, B. Zhao, J. Zhang, C. Liu, M. Chen, S. Chen, S. Banerjee, and D. Umstadter, High-order multiphoton Thomson scattering, Nat. Photon. **11**, 514 (2017).

[58] J. M. Cole, K. T. Behm, E. Gerstmayr, T. G. Blackburn, J. C. Wood, C. D. Baird, M. J. Duff, C. Harvey, A. Ilderton, A. S. Joglekar, K. Krushelnick, S. Kuschel, M. Marklund, P. McKenna, C. D. Murphy, K. Poder, C. P. Ridgers, G. M. Samarin, G. Sarri, D. R. Symes, A. G. R. Thomas, J. Warwick, M. Zepf, Z. Najmudin, and S. P. D. Mangles, Experimental Evidence of Radiation Reaction in the Collision of a High-intensity Laser Pulse with a Laser-Wakefield Accelerated Electron Beam, Phys. Rev. X **8**, 011020 (2018).

[59] Y. Sakai, O. Williams, G. Andonian, A. Fukasawa, E. Hemsing, A. Marinelli, S. Barber, F. H. O'Shea, and J. B. Rosenzweig, Harmonic radiation of a relativistic nonlinear inverse Compton scattering using two laser wavelengths, Phys. Rev. ST Accel. Beams **14**, 120702 (2011).

[60] M. Uesaka, F. Sakamoto, A. Fukasawa, H. Ogino, T. Yamamoto, D. Meng, K. Dobashi, T. Miyoshi, T. Higo, M. Akemoto, and J. Urakawa, Multi-beam Compton scattering monochromatic tunable hard x-ray source, Int. J. Mod. Phys. B **21**, 559 (2007).

[61] H. Toyokawa, T. Hayakawa, T. Shizuma, R. Hajima, K. Masuda, and H. Ohgaki, Nondestructive inspection of explosive materials using linearly polarized two-colored photon beam, Nucl. Instrum. Methods, Phys. Res. A **652**, 21 (2011).

[62] I. Drebot, V. Petrillo, and L. Serafini, Two-colour x-gamma ray inverse Compton back-scattering source, EPL **120**, 14002 (2017).

[63] J. D. Jackson, *Classical Electrodynamics*, 3rd ed. (John Wiley and Sons, Inc., New York, 1999).

[64] Y. Taira and M. Katoh, Generation of optical vortices by nonlinear inverse Thomson scattering at arbitrary angle interactions, Astrophys. J. **860**, 45 (2018).

[65] F. Ciocci, G. Dattoli, L. Giannessi, A. Torre, and G. Voykov, Analytic and numerical study of two-frequency undulator radiation, Phys. Rev. E **47**, 2061 (1993).

[66] C. Sauteret, D. Husson, G. Thiell, S. Seznec, S. Gary, A. Migus, and G. Mourou, Generation of 20-TW pulses of picosecond duration using chirped-pulse amplification in a Nd:glass power chain, Opt. Lett. **16**, 238 (1991).

[67] C. Danson, D. Hillier, N. Hopps, and D. Neely, Petawatt class lasers worldwide, High Power Laser Sci. Eng. **3**, e3 (2015).

[68] M. N. Polyanskiy, M. Babzien, and I. V. Pogorelsky, 100-terawatt CO_2 laser: Design and current status, *Advanced Accelerator Concepts 2014: 16th Advanced Accelerator Concepts Workshop, San Jose, CA, 13–18 July 2014*, edited by

Mark J. Hogan, AIP Conf. Proc. No. 1777 (AIP, Melville, NY, 2016), p. 110006.

[69] P. Sprangle and E. Esarey, Interaction of ultrahigh laser fields with beams and plasmas, Phys. Fluids B: Plasma Phys. **4**, 2241 (1992).

[70] P. Sprangle, A. Ting, E. Esarey, and A. Fisher, Tunable, short pulse hard x-rays from a compact laser synchrotron source, J. Appl. Phys. **72**, 5032 (1992).

[71] E. Esarey, P. Sprangle, A. Ting, and S. K. Ride, Laser synchrotron radiation as a compact source of tunable, short pulse hard x-rays, Nucl. Instrum. Methods, Phys. Res. A **331**, 545 (1993).

[72] S. Sasaki and I. McNulty, Proposal for Generating Brilliant X-ray Beams Carrying Orbital Angular Momentum, Phys. Rev. Lett. **100**, 124801 (2008).

[73] J. Bahrdt, K. Holldack, P. Kuske, R. Müller, M. Scheer, and P. Schmid, First Observation of Photons Carrying Orbital Angular Momentum in Undulator Radiation, Phys. Rev. Lett. **111**, 034801 (2013).

[74] M. Katoh, M. Fujimoto, N. S. Mirian, T. Konomi, Y. Taira, T. Kaneyasu, M. Hosaka, N. Yamamoto, A. Mochihashi, Y. Takashima, K. Kuroda, A. Miyamoto, K. Miyamoto, and S. Sasaki, Helical phase structure of radiation from an electron in circular motion, Sci. Rep. **7**, 6130 (2017).

[75] T. Kaneyasu, Y. Hikosaka, M. Fujimoto, H. Iwayama, M. Hosaka, E. Shigemasa, and M. Katoh, Observation of an optical vortex beam from a helical undulator in the XUV region, J. Synchrotron Radiat. **24**, 934 (2017).

[76] P. Rebernik Ribič, B. Rösner, D. Gauthier, E. Allaria, F. Döring, L. Foglia, L. Giannessi, N. Mahne, M. Manfredda, C. Masciovecchio, R. Mincigrucci, N. Mirian, E. Principi, E. Roussel, A. Simoncig, S. Spampinati, C. David, and G. De Ninno, Extreme-Ultraviolet Vortices from a Free-Electron Laser, Phys. Rev. X **7**, 031036 (2017).

[77] D. Iracane and P. Bamas, Two-frequency Wiggler for Better Control of Free-electron-laser Dynamics, Phys. Rev. Lett. **67**, 3086 (1991).

[78] G. Dattoli and G. Voykov, Spectral properties of two-harmonic undulator radiation, Phys. Rev. E **48**, 3030 (1993).

[79] C. Basu, Y. Choyal, G. Mishra, and A. K. Dutta, Analysis of two undulator radiation with low energy correction, Nucl. Instrum. Methods, Phys. Res. A **388**, 273 (1997).

[80] G. Dattoli, V. V. Mikhailin, P. L. Ottaviani, and K. V. Zhukovsky, Two-frequency undulator and harmonic generation by an ultrarelativistic electron, J. Appl. Phys. **100**, 084507 (2006).

[81] G. Dattoli, N. S. Mirian, E. DiPalma, and V. Petrillo, Two-color free-electron laser with two orthogonal undulators, Phys. Rev. ST Accel. Beams **17**, 050702 (2014).

[82] *Synchrotron Radiation Sources - A Primer*, 1st ed., edited by H. Winick (World Scientific, Singapore, 1994).

[83] F. Pacini, Rotating neutron stars, pulsars and supernova remnants, Nature (London) **219**, 145 (1968).

[84] Y. Lyubarsky, Electron-ion coupling upstream of relativistic collisionless shocks, Astrophys. J. **652**, 1297 (2006).

[85] G. Dattoli, L. Giannessi, L. Mezi, and A. Torre, Theory of generalized Bessel functions, Nuovo Cimento B (1971–1996) **105**, 327 (1990).

[86] G. Dattoli, A. Torre, S. Lorenzutta, G. Maino, and C. Chiccoli, Theory of generalized Bessel functions. II, Nuovo Cimento B (1971–1996) **106**, 21 (1991).

[87] G. Dattoli and A. Torre, *Theory and Applications of Generalized Bessel Functions*, 1st ed. (ARACNE editrice S.r.l., Roma, 1996).